Coastal Dynamics 2017
Paper No. 138

QUANTIFYING TWO-DIMENSIONAL WAVE BREAKING DISSIPATION IN THE SURF ZONE

Harold Díaz[1] and Patricio A. Catalán[2]

Abstract

In this work, we present the analysis of joint microwave and optical remote sensing data from the surf zone, aimed to estimate two-dimensional wave breaking energy dissipation fields. Breaking dissipation is derived from geometrical parameters estimated from the signature of wave breaking on each sensor, on a wave-by-wave basis. By means of a tracking algorithm, individual wave propagation paths are also determined. Individual estimates are ensemble to derive overall dissipation fields. As a method of validation, spatial gradients of these dissipation fields are computed and correlated with vorticity forcing, which in turn are compared with the location and occurrence of rip currents. Although qualitative, a good correspondence is found. This is considered indicative of the good capabilities of the method.

Key words: Hydrodynamics, Breaking dynamics, Coastal Engineering, Remote Sensing, FRF.

1. Introduction

The nearshore is the narrow portion of the oceans in contact with the continental lands. Despite its relatively limited extent, it is an extremely dynamic area where hydrodynamic and morphodynamic process interact at a wide range of temporal and spatial scales. At the same time, is one of the areas of most dear to humans, for reasons that span from recreational to economic activities. Its understanding is relevant for many aspects of human endeavors.

An essential element in this understanding are the nearshore hydrodynamic processes. Although several temporal and spatial scales can be considered, nearshore hydrodynamics are strongly influenced by process at the time scale of waves. An important process is the dissipation of organized wave energy, which results not only in the attenuation of waves as they propagate, but also transfers momentum from the wave organized motion to wave-induced mean quantities. Relevant among these mean quantities are the forcing term of mean flows (i.e. currents and circulation patterns, e.g. *Bonneton et al*, 2010) and changing in mean water levels. (e.g. *Longuet-Higgins and Stewart*, 1964; *Longuet-Higgins*, 1970). The importance of wave energy dissipation led *Holman and Haller* (2013) to argue that a direct measurement of wave energy dissipation is equivalent to measuring the mean flow forcing in the nearshore. Therefore, a robust methodology to estimate wave dissipation is required.

Although energy dissipation is due to several processes, the most relevant in the nearshore is the wave breaking process. The wave breaking process is perceived by an observer due to the generation of noise and moisture in the air, but specially by the formation of the wave roller (the turbulent body of air and water that propagates with the breaking wave *Duncan*, 1981; *Svendsen*, 1984a). The signal of wave breaking is prominent in many remote sensing modalities, such as acoustic (Melville et al., 1988), optical (Holman and Stanley, 2007), microwave (Catalán et al., 2014), and infrared (Jessup et al., 1997). One relevant advantage of these type of measurements is its synoptic and large spatial coverage.

On the other hand, a general formulation to estimate the roller induced dissipation relies on a relationship between the local geometrical parameters such as the wave height and the roller cross-sectional area A. (*Svendsen*, 1984b, and later *Nairn et a.l*, 1990; *Stive and de Vriend*, 1994, *Dally and Brown*, 1995). Some of

[1]Departamento de Obras Civiles Universidad Técnica Federico Santa María, Valparaíso, Chile. Harold.diazm@alumnos.usm.cl
[2]Associate Professor, Departamento de Obras Civiles Universidad Técnica Federico Santa María, Valparaíso, Chile. Patricio.catalan@ usm.cl

these parameters are observable by a range of remote sensing modalities, which have allowed the estimation of the local dissipation due to breaking (*Haller and Catalán*, 2009, *Díaz Mendez et al.,* 2015, *Carini et al., 2015*). Moreover, *Flores et al.*, (2016) estimated the one-dimensional forcing of mean water level by coupling estimates of wave breaking dissipation (from remote sensing) and a phase averaged model based on the roller formulation.

One notable aspect to all these recent roller-related efforts is that they have been performed for one-dimensional (cross-shore) wave breaking. Expansion to two dimensional is desirable, because the hydro-dynamics grow in complexity and the most conspicuous result of the two-dimensional wave fields is the development of nearshore circulation. Alongshore discontinuities or variability in wave breaking dissipation can induce vertical vorticity which manifests itself as macro-vortices that could, in turn, develop in rip currents. Mean flow vorticity is directly forced by wave breaking dissipation (e.g. *Bühler and Jacobson* 2001, *Bonneton et al.,*2010)

$$\frac{\partial \bar{\omega}}{\partial t} + \nabla\left(\bar{\omega}\overrightarrow{\mathbf{U}}\right) = \nu_t \nabla^2 \bar{\omega} + \nabla \times (D_r e_k) \tag{1}$$

where ω is the mean vertical vorticity, $\mathbf{U}^{\rightarrow}$ is the mean transport velocity (current and waves), νt is an horizontal mixing coefficient, and D is the wave breaking induced dissipation. Eq. 1 shows that the total rate of change of vorticity (the left-hand side) is accounted for a mixing term and only one forcing term, which is directly dependent on D. Therefore, it is apparent that estimation of 2D dissipation fields from remote sensing data can be relevant for understanding

In this work, we intend to develop the algorithmic basis to estimate 2D dissipation fields, and qualitative validate the results against an indirect measure of circulation, such as the presence of rip currents. To this end, we use the methodology proposed by *Catalán et al.,* (2011) to estimate the two-dimensional wave breaking fields. Next, a roller model (*Duncan,* 1981; *Svendsen, 1984a*) is used to estimate energy wave dissipation fields on a wave-by-wave basis. These in turn, are used to estimate the main forcing in Eq. (1) which will be then correlated with rip currents.

The paper is organized as follows: in section 2 a review of the relationship between wave breaking roller and circulation patterns is presented. Section 3 describes shortly the experimental data used. Data processing procedures and breaking detection are concisely presented in section 4. In section 5 main results and an alternative validation are disclosed. And finally, section 6 present a short discussion about the results and future work perspectives.

2. Theory and Methodology

To estimate the 2D dimensional dissipation fields, a first step is to correlate remote sensing observables with wave breaking dissipation. This is achieved by a 1D dissipation model. Next, the local 1D estimates need to be translated to 2D. These steps are reviewed in the following

2.1 Duncan Model and Dissipation Measurements (D81)

Duncan (1981), (here in after D81), proposed a model of single wave energy dissipation where the roller dissipation is estimated from the work done by the shear stress acting on the interface between the roller and the underlying wave. In turn, the weight of the roller must be balanced by the shear stress for a force balance to exist, then the time-averaged rate of energy dissipation per unit planform area into the direction of roller motion (e_k, where e_k is the unitary vector along the wavenumber direction) reads (*Duncan*, 1981, *Dally and Brown*, 1995)

$$D_r = \frac{\rho_I g A \sin\theta \cos\theta}{T}\left[\frac{Watt}{m^2}\right], \tag{2}$$

where ρ' is the average densitiy of the roller (here assumed constant and equal to 60% of the sea water density,

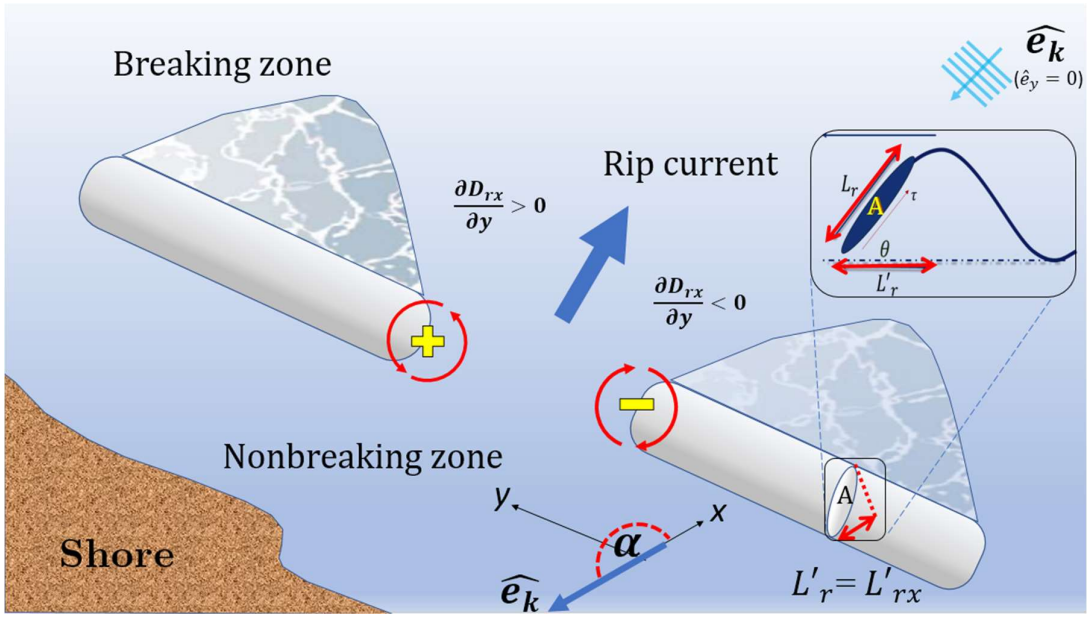

Figure 1. Scheme of nonhomogeneous wave breaking in the nearshore, describing principal features of wave breaking roller and rip formation.

following *Carini et al*., 2015), A is the cross-sectional area of the roller and T is the wave period and θ is the inclination angle of the roller, which controls the amount of wave energy storage in the roller and its size. (see inset in Fig. 1). Thus, the energy dissipation its controlled by wave geometry. D81 observed that the roller geometry is self-similar through most of its life cycle

$$A/{L_r}^2 = 0.11 \mp 0.01, \tag{3}$$

where L_r is the along-slope length of the roller. Assuming θ is known, it is possible to relate the horizontal projection of L_r, a remote sensing observable, to L_r, as $L_r = {L'}_r/cos(\theta$. Hence, a local (in space and time), across-wave estimate of the dissipation can be obtained.

To estimate 2D fields, it is assumed that most of energy dissipation occurs in the front face of the wave where most of the spreading take place. All alongwave dissipation is thus discarded. A dissipation vector can be thus constructed by projecting the across-wave dissipation into a global reference frame. As a wave propagates with an incidence angle α, referred to the local system shown in Figure 1, the local across-wave length can be expressed as a function of its geometrical components ${L'}_{rx}={L'}_r|\cos(\alpha)|$, ${L'}_{ry}={L'}_r|\sin(\alpha)|$.

The case shown in Figure 1 represents the case studied in this paper. When waves reach the coast, their propagation vector its almost perpendicular to shore, then the component of ${L'}_r$ in the *y-axis* is practically equals to zero (sin(180º) ~ 0) (this fact will be supported by the results obtained in the sections below). The previous result allows us to consider just the *x-axis* component of the wave energy dissipation in the 2D analysis. Combination of (2), (3) and geometrical relationships, yields

$$D_r \approx D_{rx} = \frac{0.11\rho g({L'}_r * |\cos(\alpha)|)^2 \tan(\theta)}{T} \left[\frac{Watt}{m^2}\right] \tag{4}$$

Although we recognize that θ varies in time and space, here is considered as time-independent and cross-shore constant.

Estimates of dissipation can be thus obtained on a wave-by-wave basis, and mapped into the computational grid by scaling the dissipation per unit area by the grid element area.

2.2 Bonneton et al., (2010) Circulation Model

Validation of these results is difficult because no other sensor can provide two-dimensional dissipation fields. Hence, we use a proxy approach, where we take advantage of the relevance of wave breaking dissipation in the development of near shore circulation. Specifically, a simplified Eq. (1), by neglecting the horizontal mixing term

$$\frac{\partial \bar{\omega}}{\partial t} + \nabla(\bar{\omega}\bar{u}) = \nabla \times (D_r e_k) \tag{5}$$

$$\frac{\partial \bar{\omega}}{\partial t} + \nabla(\bar{\omega}\bar{u}) = (\mp \frac{\partial D_{ry}}{\partial x} + \frac{\partial D_{rx}}{\partial y}); e_z \tag{6}$$

is used, where $\bar{\omega}$ is the mean vertical vorticity and D_r is, the wave breaking induced dissipation vector. Eq. (5) shows that the total rate of change of vorticity is accounted for by one forcing term, which is directly dependent on D_r (e.g. *Bonneton et al*., 2010*, Clark et al*., 2012). In turn, one of the main manifestations of nearshore circulation is the development of rip currents, which occurs frequently in the presence of non-homogeneous alongshore distributions of wave breaking. In Fig. 1 the main mechanism or rip formation is shown, where opposing spatial gradients in dissipation interact constructively to feed the rip. Hence, we will use the presence of a rip current as a proxy to correlate with our forcing estimates. To this end, we take advantage that rips currents can also be imaged by remote sensors (e.g. *Haller et al*., 2014) and were observed during in our data.

3. Experimental Data

To develop and validation of this methodology, data from two different field experiments at U.S. Army Corp of Engineers Field Research Facility (FRF), Duck, NC have been used. The FRF coordinate system is used, where the cross-shore coordinate is denoted as *x* and points offshore, the *y* axis points roughly 18º west from north, and z = 0 correspond to NADV29. For the data analyzed herein, the shoreline was located at approximately *x* = 90 [m] in FRF coordinate system. Despite several instruments where deployed in during the experiments, we concentrated in data provided from two remote sensing sensors. The first one was a single polarization (HH) marine radar (Si-Tex RADARpc-25.9) operating at 9.45 GHz. The radar antenna was mounted atop of a 10-m tower near the north end of FRF facility (x=17.4 [m], y=971.4 [m] and z=13.8 [m]). The marine radar is in active sensor with a 25-kW nominal power and 9-fit open array antenna that rotates at approximately 44 rpm (see Catalán et al., 2011, for details). The second remote sensing system was comprised of three optical cameras from the ARGUS III observing station, further details of this system can be found in *Holman and Stanley* (2007).

For data acquisition and post processing, a regular pixel array has been used, spanning *x*=60-600 [m] and *y*=500-1000 [m], with a spatial resolution of $\Delta x = 2$ [m] and $\Delta y = 5$ [m], using field view of cameras 0, 3 and 1 for both remote sensing sensors, as shown in Fig. 2. To analyze the synchronous instantaneous signals from the two sensors, the differences in sampling rates and spatial resolution were removed by interpolation to a common domain. Although we use three cameras of the ARGUS III system, boundaries between camera's field of view have been avoided due the difference in gain leading to a sharp gradient not related with the ocean surface (see Fig. 2, boundaries as dotted white lines).

Two datasets are used. The first from the Multi Remote SENsing Surfzone Observations (MR-SENSO) starting May 14, 2008 18:00 GMT with a duration of 27 min, hereinafter run1. The second dataset was taken from Surf Zone Optics Experiment (SZO) starting Sep 9, 2010 17:59 GMT with a duration of 15 min,

hereinafter run2. It is worth to mention that run2 was among those used by *Haller et al.*, (2014) to demonstrate that rip current can be detected by radar signal induced using a crosscheck between the radar signal and the current meter deployed in situ. Wave conditions varied between the two datasets, from relatively energetic swell at mid tide, to a less energetic wind sea at low tide as shown in Table 1. The latter conditions were favorable for imaging the rip current, whereas no rip was present for the first run. As can be seen in Fig. 2, run1 had a wider surf zone with offshore breaking above a bar, whereas run2 had a much narrower surf zone with concentrated breaking over a bar.

Table 1. Summary of wave conditions

	Tp (*s*)	Hs (*m*)	MWD (FRF)	Tide(m)
Run1	**12.7**	**1.9**	**5º**	**0.7 (Mid tide)**
Run2	**5.8**	**0.7**	**-22º**	**-0.1 (Low tide)**

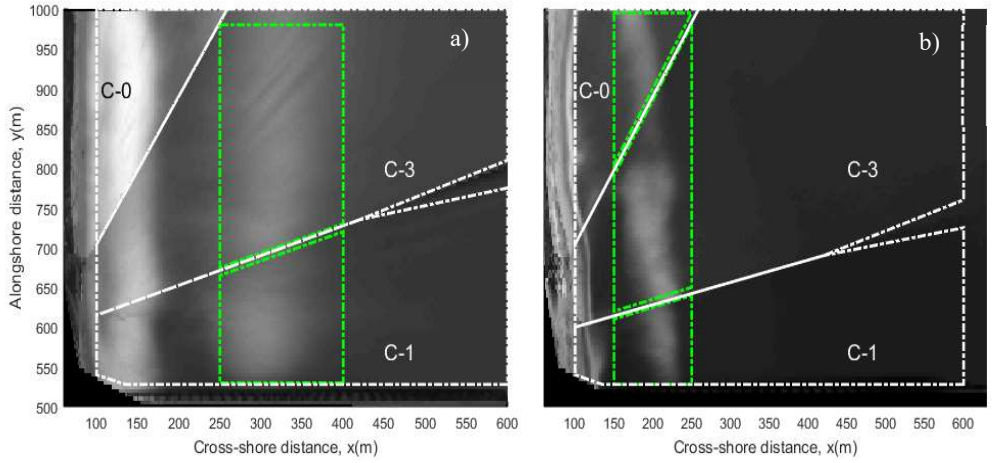

Figure 2. Field of view of each cam in both runs a) run1, b) run2. Boundaries between cameras are shown in dashed-dotted white line. Green dashed-dotted line shows the breaking region of interest. C-0 – C-1 – C-3 indicate the camera number in the ARGUS system.

4. Data Processing and Breaking Detection

Data consists in time series of optical pixel intensity and radar intensity over the whole domain. This allows processing on a frame by frame basis. In addition, several simultaneous breaking events can occur and it is necessary to account for the evolution of each breaking event across several frames.

To discriminate breaking waves, the joint-pdf approach of *Catalan et al*., (2011) has been updated with the automatic threshold selector proposed *by Carini et a.l*, (2015) for the video data (final values used are shown in Table 1) and a constant value of -28dB for the radar. Fig. 3 shows a sample of the detection, where green correspond to steep waves, cyan to remnant foam and red for wave breaking roller. A very good detection ability can be observed.

Table 2. Video pixel intensity thresholds.

	Cam0	Cam1	Cam3
Run1	**-**	**85**	**89**
Run2	**103**	**80**	**103**

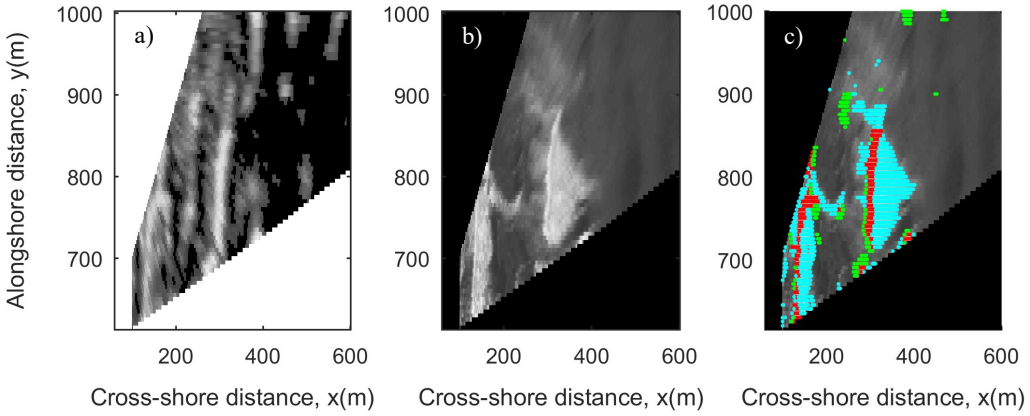

Figure 3. Detection scheme in cam3 field of view, run1 a) Radar snapshot b) Video snapshot c) Breaking (red), steep(green) and foam(cian) mask over video snapshot.

After isolating breaking areas in each frame, a tracking technique is used to follow the time history of each individual breaking event. This allows estimation of their propagation angle, event duration and the rate of events occurring on each frame. The tracking is based in a mean wave celerity criteria, where events in two consecutive events are considered the same if their centroid had moved at a velocity smaller $C_x = 10\ [m/s]$; $C_Y = 3.5\ [m/s]$; $\|C\| = 10.5\ [m/s]$. As an example, Fig. 4 shows the evolution of single event. In panel 4b), it can be seen the cross-shore propagation of the event but also its lateral spreading. Panel 4c) shows the local displacement of the centroid (frame by frame), whereas the green arrow shows the total variation in position since wave breaking began. The centroid wobbles in the alongshore direction, due to the roller changing its size. However, these variations do not affect the overall propagation direction of the wave, which is the quantity of interest.

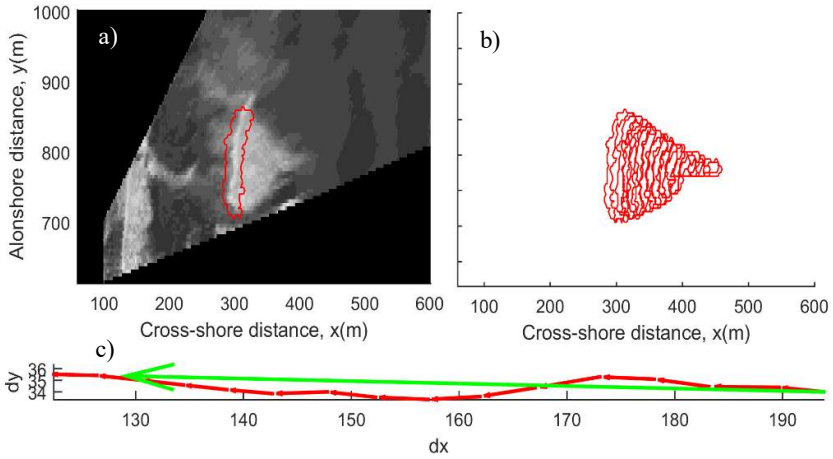

Figure 4. Tracking technique scheme a) Video snapshot with the breaking roller event marked in red line b) Footprint left by roller c) local and total roller centroid displacement, red and green arrow respectively

With the dissipation at the wave front, along the entire roller front, and the wave direction angle, it is possible to construct a space-time map of the dissipation vector (referred to the FRF coordinate system). Spatial gradients and curl can be then estimated in a straightforward manner.

5. Results

5.1 Roller Length and Breaking Properties

The total number of correctly isolated events in run1 was 1740 (62 events/min) with an average life span of 6 [s]. On the other hand, run2 presented 1544 events (102 events/min) with an average duration of 4[s]. These results are consistent with the wave conditions observed, in the sense that the longer period waves of run1 break less frequently but have longer time spans than those in run2.

The statistical analysis of the propagation vector estimation, performed over all individual events, shows a normal distribution of incidence angles (not shown), with mean (standard deviation) of 179.8º (6,6º) and 181º (11º), for runs 1 and 2, respectively. Both mean incidence angles are close to shore normal in the coordinate system used, hence the alongshore projection of the dissipation vector can be discarded.

The average roller length measured in run1 was 14[m] and its mean series values shows a slight modulation (Figure 6 a). On the other hand, no signs of modulation have found in run2 with a mean length of 6 [m], although longer roller lengths can be seen as episodic.

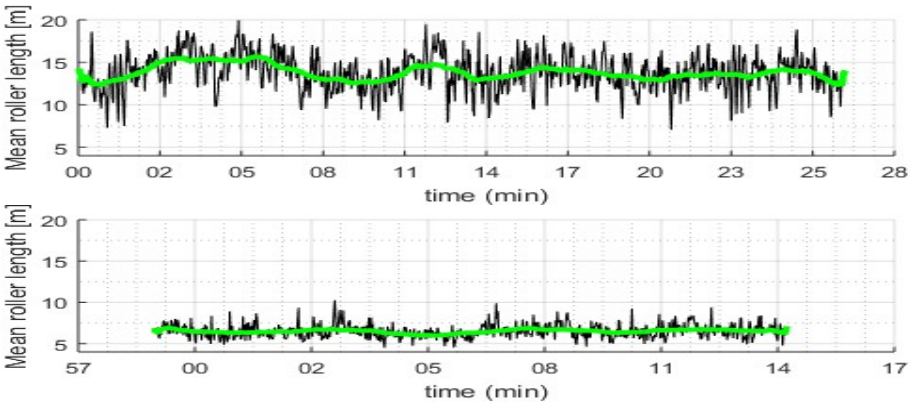

Figure 6. Mean roller length over all frames a) run1 b) run2

5.2 2-D Energy dissipation fields

The model uses as single free parameter the wave front slope angle, which is assumed fixed with a value of 8º, consistent with the 2 – 24º range reported in the literature from both laboratory and field experiments (*Duncan*, 1981; *Dally and Brown*, 1995; *Reniers and Battjes*, 1997; *Ruessink et al.*, 2001; *Haller and Catalan*, 2009, *Carini et al*., 2015).

Spatio-temporal maps of dissipation are constructed. However, individual frames of dissipation do not show a clear structure, therefore, a moving average technique was applied, with different averaging windows. In Fig. 7, the effect of the averaging can be observed. Panels a) and b) show averaging over $1T_p$, where individual events leave a clear dissipation signature, and sharp gradients can be observer throughout the image. Panels c) and d) show averaging over $100T_p$, where additional structures become apparent. Run1 shows an homogenous dissipation structure over the sandbar, with no significant gradients over the domain. Run2 instead shows a non-homogenous behavior over the sandbar, which creates large gradients specially in the range y = 800-950 [m]. It is important to mention that the reduced breaking in that location coincides with the rip neck position determined by *Haller et al*., (2014), suggesting a possible correlation. The sharp gradient close to y=600 m is an artifact of the camera boundary.

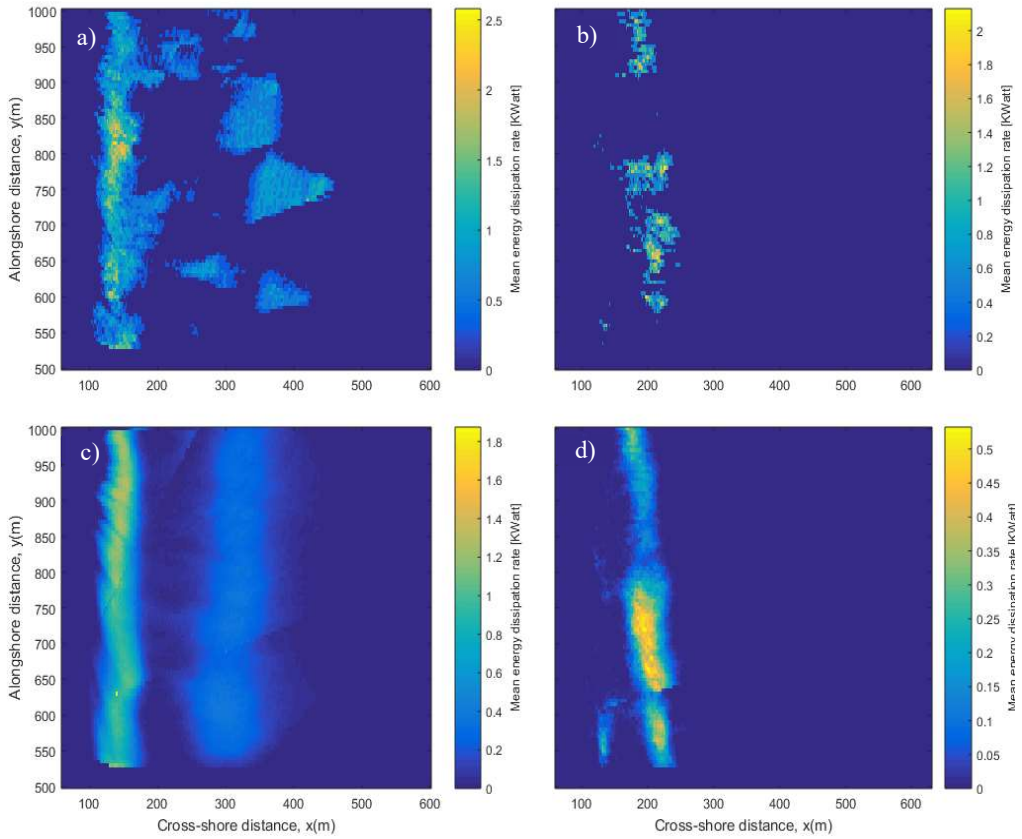

Figure 7. Dissipation maps a) and c) run1 for $1T_p$ and $100T_p$ respectively. b) and d) run2 for $1T_p$ and 100 T_p respectively

These results show that it is necessary to estimate the forcing at time scales longer than the individual wave period, but relatively short to allow for estimating changes in the wave field (Macmahan et al., 2006) In what follows, we use arbitrarily $10T_p$.

5.3 Vorticity forcing estimates

The curl of the dissipation field is estimated and averaged over this time span, which in accordance to Eq. 5, should give an estimate of the vorticity forcing. In Fig. 8 a), the radar time exposure shows energetic breaking but no clear presence of a rip for run1. This is in good correspondence with the curl of dissipation over (Fig. 8 b) where positive and negative forcing are spread rather homogeneously over the surf zone. While some adjacent areas of positive and negative dissipation curl are present, the values are generally small. This structure is persistent in time and constant in space, during the 28 minutes of run1. In contrast, run2 (Fig. 8c

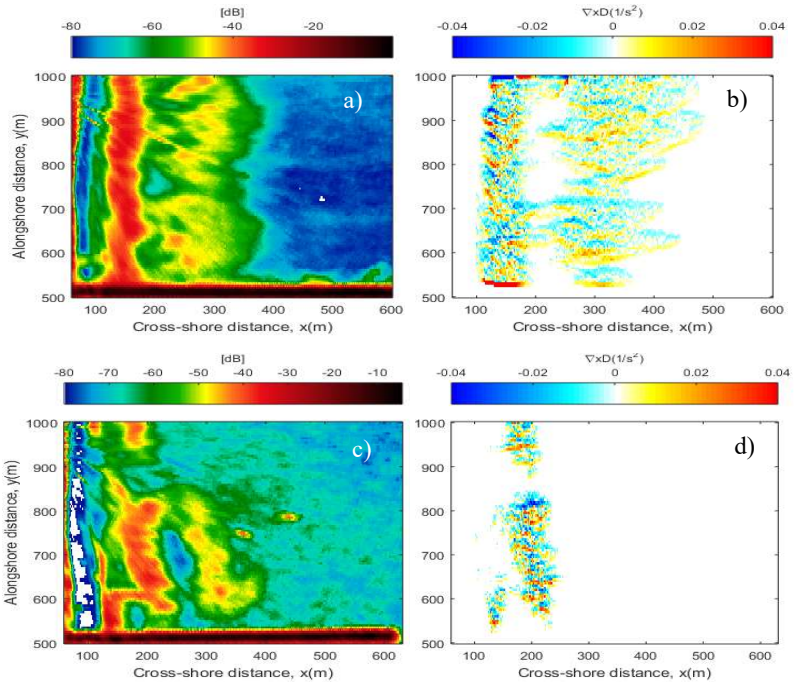

Figure 8. a) and c) 10 T_p radar timex for run1 and run2 respectively. b) and d) 10T_p averaged curl of dissipation field for run1 and run2 respectively

and d) shows a large gap in the curl of dissipation near *y*=850 m, and a doublet of dissipation curl with values that at least double those found in run1. Both elements coincide with the rip neck, consistently to what was expected to find by the dissipation curl, assumed to be equivalent to the dissipation forcing.

6. Discussion

The validation of these results is not an easy task, because it requires a dense array of measurements to account for either the dissipation production, or for the velocity field from which the circulation can be derived (e.g. *Clark et al.,* 2012). Alternatively, it could be possible to compare these results against modeling results, but this will be the subject of future work. In what follows, considering the promising results obtained, we optimistically analyze what other products can be obtained from the data analysis.

6.1 Vorticity forcing term evolution

Considering that a moving average of vorticity forcing is estimated, it is possible to analyze the space-time evolution of it. Consequently, a space-time map is constructed by averaging in space (across the cross-shore extent of the breaking zones shown in Fig.2) and time (10 T_p steps). As a result, the evolution of the forcing term over an alongshore transect is estimated. Fig. 9 shows the results for both runs, where a time-space map is shown in panels a) and c), and individual instances of vorticity forcing are shown in panels b) and d) (gray lines), and the overall run average is shown by the red line.

Run1 exhibits a relatively random behavior in time with episodic instances of positive and negative forcing at the same alongshore location, with no clear identification of a spot of sustained vorticity forcing. Peak forcing values vary in the alongshore, but the average forcing exhibits a relatively uniform alongshore distribution. An exception to this trend occurs near *y*=525 [m] where higher values is present. However, this is an artifact due to the Duck pier affecting the image processing algorithm. border which disturb the signal

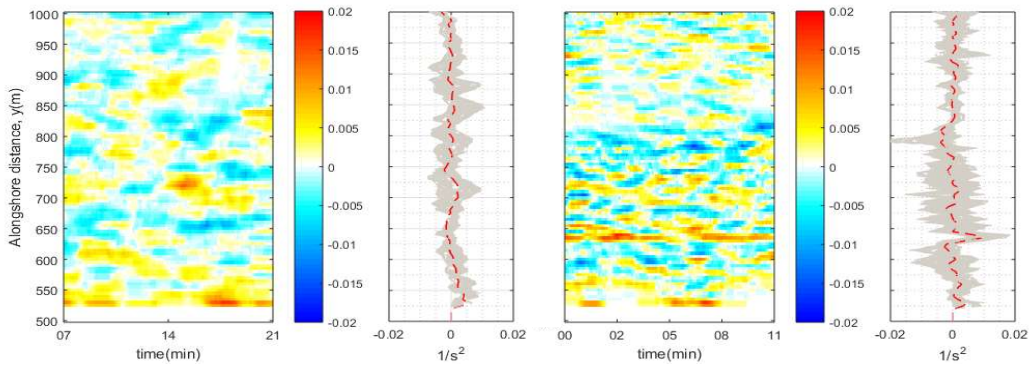

Figure 9. a) and c) Vorticity forcing term timestack for run1 and run2 respectively. b) and d) collapsed time averaged of timestack for run1 and run2 respectively.

and generate big artificial gradients. The mean vorticity forcing profile shows variations about zero value, although a local patch of large vorticity is present near *y*=700-750 m, apparently induced by an isolated event near *t*=15 min.

Although run2 also shows a large degree of variability, some characteristic trends are more apparent than in the case of run1. For instance, between *y*=800-850 m, the forcing term shows very low values, whereas northward of this region the forcing tends to have an alternating behavior. South of it, in the region *y*=750-800 m, the forcing is markedly negative, with some episodic large magnitude events. South of this region, the behavior is again oscillatory, but with larger extrema than in the northern area. There is also a narrow section of consistently large forcing near y=625 m. The gap and negative-positive pair near *y*=850 m is consistent with the schematic shown in Fig. 1., and suggests a forcing persistence leading to the development of the rip. On the other hand, the narrow positive-negative pair near *y*=625 m could not be correlated with any feature on the radar image.

As expected, the results show that the magnitude of the forcing term is not directly coupled with the dissipation structure or the energy of the incoming field (see Fig. 8), but with the gradients of dissipation. As a result, the magnitude of the forcing term is nearly doubled between runs.

6.2 Bulk Energy and dissipation comparison

Although no direct assessment can be made on the accuracy of the vorticity forcing estimates, it is possible to perform a comparison between the incoming bulk energy flux and energy dissipation estimated. This allows the estimation of the ratio of energy being dissipated in the surf zone. In addition, considering that wave front slope angle is the only free parameter, we also analyze the dependence of the results on its value.

The bulk energy flux incoming is calculated by integrating the density energy spectrum times the frequency-dependent group velocity,

$$\mathcal{F} = \int E(f) * c_g(f)\, df \tag{6}$$

Fig. 10 shows the time evolution of the ratio $D_{81}/\mathcal{F}$, where the $D_{81}/\mathcal{F}$=1 represent that all the incoming energy is being dissipated. The black line corresponds to dissipation estimates obtained here, where on average, nearly 50% of the incoming energy is being dissipated over the bar. The remainder of energy can be dissipated in the shoreline break, or it can be reflected. The shaded areas correspond to dissipation estimates obtained by changing the wave front slope angle within the range 2-14º. A large sensitivity to this parameter is observed, highlighting the relevance of having actual measurements of it.

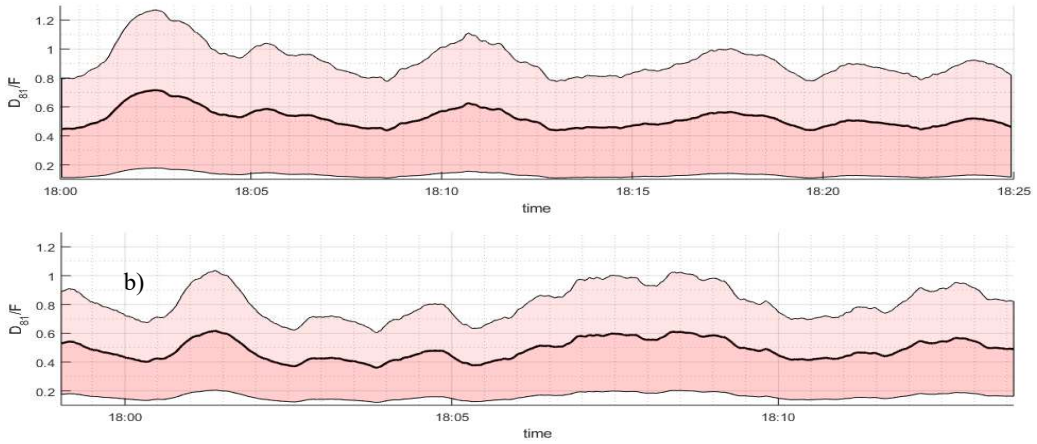

Figure 10. a) run1 and b) run2, energy ratio over run's time for the range of roller inclination angles selected. Black highlight line represents the energy ratio calculated with mean roller inclination angle in the range selected. Upper and lower black line, energy ratio calculated with the extreme θ values.

7. Conclusions

The objective of the present study was to develop a methodology to estimates the 2-D dissipation fields from remote sensing data. Although derived from a fusion of optical and microwave data, the methodology is independent of the sensing technique used provided it is possible to discriminate the active breaking portion of each wave. Unfortunately, no direct data were available to validate the results. Hence, we adopted a qualitative approach by means of estimating the spatial gradients of the dissipation patterns observed, and compared them with the occurrence of rips. A good correspondence was found, both as an average and as time series.

Although largely exploratory at this stage, deriving time series of dissipation fields from remote sensing data offers the opportunity to shed more light in the understating of the development of circulation, for instance, or real-time monitoring. However, more work is required to provide a thorough validation of these results.

References

Bonneton, P., N. Bruneau, B. Castelle, and F. Marche (2010), Large-scale vorticity generation due to dissipating waves in the surf zone, *Discrete and Continuous Dynamical Systems - Series B*, *13*(4), 729–738.

Bühler, O., and T. E. Jacobson (2001), Wave-driven currents and vortex dynamics on barred beaches, *Journal of Fluid Mechanics*, *449*, 313–339.

Carini, R. J., C. C. Chickadel, A. T. Jessup, and J. Thomson (2015), Estimating wave energy dissipation in the surf zone using thermal infrared imagery, *Journal of Geophysical Research: Oceans*, *120*(6), 3937–3957.

Catalán, P. A., M. C. Haller, R. A. Holman, and W. J. Plant (2011), Optical and microwave detection of surf zone breaking waves, *IEEE Transactions on Geoscience and Remote Sensing*, *49*(6), 1879–1893.

Catalán, P. A., M. C. Haller, and W. J. Plant (2014), Microwave backscattering from surf zone waves, *Journal of Geophysical Research*, *119*(5), 3098–3120.

Clark, D. B., S. Elgar, and B. Raubenheimer (2012), Vorticity generation by short-crested wave breaking, *Geophysical Research Letters*, *39*(24)

Dally, W. R., and C. A. Brown (1995), A modeling investigation of the breaking wave roller with application to cross-shore currents, *Journal of Geophysical Research*, *100*(C12), 24,873–24,883.

Díaz Méndez, G. M., M. C. Haller, B. Raubenheimer, S. Elgar, and D. A. Honegger (2015), Radar remote sensing estimates of waves and wave forcing at a tidal inlet, *J. Atmos. Oceanic Technol.*, *32*(4), 842–854.

Duncan, J. (1981), An experimental investigation of breaking waves produced by a towed hydrofoil, *Proc. R. Soc. London A*, *377*(1770), 331–348.
Flores, R. P., P. Catalán, and M. C. Haller (2016), Estimating surfzone wave transformation and waves from remote sensing data, *Coastal Engineering*, *114*, 244–252.
Haller, M. C., and P. A. Catalán (2009), Remote sensing of wave roller lengths in the laboratory, *Journal of Geophysical Research*, *114*, C07,022.
Haller, M. C., D. Honegger, and P. A. Catalán (2014), Rip current observations via marine radar, *Journal of Waterway, Port, Coastal, and Ocean Engineering*, *140*(2), 115–124.
Holman, R., and M. C. Haller (2013), Remote sensing of the nearshore, *Annual Review of Marine Science*, *5*(1), 95–113.
Holman, R., and J. Stanley (2007), The history and technical capabilities of Argus, *Coastal Engineering*, *54*, 477–491.
Jessup, A. T., C. J. Zappa, M. R. Loewen, and V. Hesany (1997), Infrared remote sensing of breaking waves, *Nature*, *385*, 52–55.
Longuet-Higgins, M. S. & Stewart, R. Radiation stresses in water waves; a physical discussion with applications Deep Sea Research, 1964, 11, 529-562
Longuet-Higgins, M. S. Longshore currents generated by obliquely incident sea waves: 1, *Journal of Geophysical Research*, 1970, 75, 6778-6789
MacMahan, J. H.; Thornton, E. B. & Reniers, A. J. Rip current review, *Coastal Engineering*, 2006, 53, 191-208
Melville, W. K., M. R. Loewen, F. C. Felizardo, A. T. Jessup, and M. J. Buckingham (1988), Acoustic and microwave signatures of breaking waves, *Nature*, *336*, 54–56.
Nairn, R. B., J. Roelvink, and H. N. Southgate (1990), Transition zone with and implications for modelling surfzone hydrodynamics, in *Proceedings, 22th International Conference on Coastal Engr.*, pp. 68–81, ASCE.
Reniers, A. & Battjes, J.A laboratory study of longshore currents over barred and non-barred beaches Coastal Engineering, 1997, 30, 1-22
Ruessink, B. G., J. R. Miles, F. Feddersen, R. T. Guza, and S. Elgar (2001), Modeling the alongshore current on barred beaches, *Journal of Geophysical Research*, *106*(C10), 22,451–22,463.
Stive, M. J., and H. J. De Vriend (1994), Shear stresses and mean flow in shoaling and breaking waves, in *Proceedings, 24th International Conference on Coastal Engr.*, pp. 594–608, ASCE.
Svendsen, I. A. (1984a), Mass flux and undertow in the surf zone, *Coastal Engineering*, *8*, 347–365.
Svendsen, I. A. (1984b), Wave heights and set-up in a surf zone, *Coastal Engineering*, *8*, 303–329.